IOP Publishing Phys. Med. Biol. 65 (2020) 025011 (17pp) https://doi.org/10.1088/1361-6560/ab58ad

Physics in Medicine & Biology

IPEM Institute of Physics and Engineering in Medicine

PAPER

A spectral reconstruction algorithm for two-plane Compton cameras

RECEIVED
26 June 2019

REVISED
14 November 2019

ACCEPTED FOR PUBLICATION
18 November 2019

PUBLISHED
16 January 2020

Enrique Muñoz, Luis Barrientos, José Bernabéu, Marina Borja-Lloret, Gabriela Llosá, Ana Ros, Jorge Roser and Josep F Oliver

Instituto de Física Corpuscular, CSIC/Universitat de València, Valencia, Spain

E-mail: Enrique.Munoz@ific.uv.es

Keywords: Compton imaging, Compton camera, hadron therapy, image reconstruction

Abstract

One factor limiting the current applicability extent of hadron therapy is the lack of a reliable method for real time treatment monitoring. The use of Compton imaging systems as monitors requires the correct reconstruction of the distribution of prompt gamma productions during patient irradiation. In order to extract the maximum information from all the measurable events, we implemented a spectral reconstruction method that assigns to all events a probability of being either partial or total energy depositions. The method, implemented in a list-mode maximum likelihood expectation maximization algorithm, generates a four dimensional image in the joint spatial-spectral domain, in which the voxels containing the emission positions and energies are obtained. The analytical model used for the system response function is also employed to derive an analytical expression for the sensitivity, which is calculated via Monte Carlo integration. The performance of the method is evaluated through reconstruction of various experimental and simulated sources with different spatial and energy distributions. The results show that the proposed method can recover the spectral and spatial information simultaneously, but only under the assumption of ideal measurements. The analysis of the Monte Carlo simulations has led to the identification of two important degradation sources: the mispositioning of the gamma interaction point and the missing energy recorded in the interaction. Both factors are related to the high energy transferred to the recoil electrons, which can travel far from the interaction point and even escape the detector. These effects prevent the direct application of the current method in more realistic scenarios. Nevertheless, experimental point-like sources have been accurately reconstructed and the spatial distributions and spectral emission of complex simulated phantoms can be identified.

1. Introduction

The beneficial features of hadron therapy for the treatment of certain tumors have led to a steep increase in the number of patients treated with this technique over the past years (PTCOG 2019). In order to fully exploit the dose deposition profile given by the shape of the Bragg peak, real-time treatment monitoring methods are being investigated (Krimmer *et al* 2018). The research for real-time monitoring devices for dose delivery in hadron therapy is based on the detection of secondary particles produced during irradiation, mainly positrons and prompt gammas, and the reconstruction of the positions where they are created, which can be correlated to the dose absorbed by the patient (Min *et al* 2006). The use of Compton cameras as dose monitors in hadron therapy has been studied by several research groups over the past few years (Frandes *et al* 2010, Peterson *et al* 2010, Kormoll *et al* 2011, Roellinghoff *et al* 2011, Kurosawa *et al* 2012, Llosá *et al* 2012, Thirolf *et al* 2016, Parajuli *et al* 2019).

The process of image formation in Compton imaging systems is based on the detection in time coincidence of two successive interactions by one incoming photon, being the first of them a Compton scatter. The positions of the two measured interactions and the energy deposited in the Compton scatter allow confining the origin of the photon to a conical surface, as long as the initial energy of the incoming photon is known.

This makes conventional Compton cameras suitable for imaging sources of gammas in the range of hundreds of keV, for which complete absorption in the second interaction has a high probability; however, full absorption becomes increasingly less likely for higher initial energies. While many previous studies in the literature present detailed models for the system matrix (SM) of two-stage Compton cameras, e.g. Wilderman *et al* (2001), Maxim *et al* (2016), Muñoz *et al* (2018), they generally assume knowledge of the gamma initial energy at the moment of reconstruction. In hadron therapy, the prompt gammas emitted during the treatment are mostly generated in the range between 1 and 7 MeV (Verburg *et al* 2013, Schumann *et al* 2015), so the assumption of either prior knowledge or full absorption of the gamma energy is not accurate in many cases. If the photon energy is not fully absorbed in the second interaction, it is possible to recover its initial energy if a third interaction is also detected (Dogan and Wehe 1994, Kroeger *et al* 2002). Nevertheless, the probability of a photon to produce three interactions in the detector is in most cases at least one order of magnitude lower than that of producing only two (Muñoz *et al* 2017), and so, given the limited particle production, the two-interaction option appears highly advantageous. The detection efficiency of Compton cameras at clinical rates is currently one of the most limiting factors for their applicability in dose monitoring, which has been specifically addressed in several published works (Golnik *et al* 2016, Rohling *et al* 2017, Draeger *et al* 2018).

Given the continuous spectrum of creation of prompt gammas and the necessity for high detection efficiency, a possible approach towards the applicability of a Compton imaging system to treatment monitoring in hadron therapy is the employment of spectral reconstruction algorithms for two-interaction events. In this work we present an approach towards the development of a spectral reconstruction algorithm, which is tested with various distributions of simulated and experimental multi-energy sources. The principle that constitutes the basis of the algorithm is the fact that the second interaction can be either a full or a partial absorption of the energy carried by the scattered photon, and so the coincidence event may have been produced by a photon with an initial energy equal or superior to the sum of the energies deposited in both interactions. This allows the formation of a set of conical surfaces with a different aperture angle for each of the initial energies tested. In turn, each conical surface is built taking into account the probability that the considered initial energy produces the measured outcome; in order to do so, the probabilities assigned to the system matrix elements are calculated as described in Muñoz *et al* (2018), with an extension to the spectral dimension. An expression for a four-dimensional sensitivity matrix has also been derived from the physical model.

An approach towards a spectral reconstruction algorithm for Compton cameras aimed to prompt gamma imaging was already proposed in Gillam *et al* (2011). Although this method did not take into account all the probabilities of the different physical processes involved, it was successfully employed in Solevi *et al* (2016) to measure shifts in the Bragg peak. A much more detailed model was presented in Xu and He (2007), which was proven to accurately reconstruct sources with spectral emission below 1 MeV. The model derived in this work is similar to the one used in Xu and He (2007), with the addition of the physical processes introduced by photons of up to 10 MeV (additional terms to account for the e^-e^+ pair production interaction), the derivation of an analytical expression for the sensitivity matrix and a specific implementation for our experimental prototype.

The paper is organized as follows. Section 2 presents in detail the analytical model for the calculation of the probabilities and the implementation of the algorithm for the computation of the SM elements. The simulated and experimental sources employed in this work to evaluate the method are also presented in this section. Section 3 shows the evaluation of the developed model and the obtained reconstructed images of the considered sources. Section 4 is dedicated to the discussion of the results from section 3, and the final conclusions are presented in section 5.

2. Materials and methods

2.1. The system matrix

When the energy of the incoming photons is known, the image reconstruction algorithm can exploit this information. However, when it is not, the reconstruction algorithm should somehow compensate for this lack of information. The approach we follow in this work is to simultaneously estimate the (spatial) distribution and the (energy) spectrum of the photons emission. To this end, we extend the method presented in Muñoz *et al* (2018), which was only applicable to the reconstruction of monochromatic sources of known energy in two aspects: first, four dimensional voxels (the three coordinates of the emission point plus the energy) are used and, second, an explicit model of the type of interaction in the second detection plane is kept.The derived model is similar to that of Xu and He (2007), but with significant differences in order to adapt it to our experimental system. In our derivation, we select the variables such that they allow us to obtain a specific expression for the sensitivity matrix, as well as make explicit the presence of the Compton cone surfaces, together with a straightforward way of numerically implementing the decomposition of these cones into a finite set of rays.

In order to obtain the expression of the SM elements of our telescope, we start by writing the probability of detection of a photon emitted from inside one of the (hyper) voxels V characterized by the position $\vec{r}_0$ and the

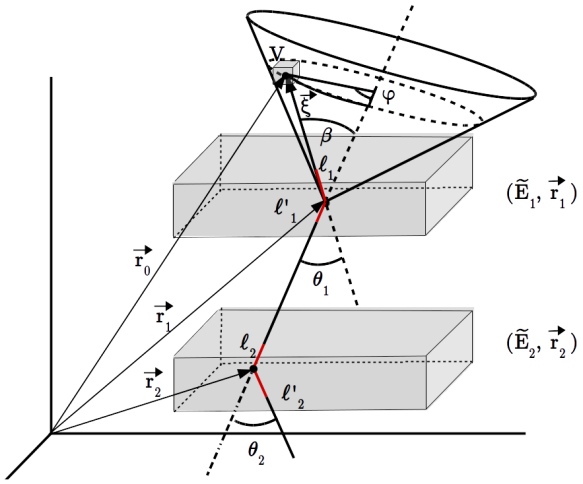

Figure 1. Diagram of an ideal Compton camera measured event. The positions of interaction and the scattering angle β define a conical surface containing the origin of the detected photon.

energy E_0, as depicted in figure 1. It should be noted that, in this work, the term V always refers to a four-dimensional (hyper) voxel with (hyper) volume $V = \Delta x \Delta y \Delta z \Delta E_0$. The probability reads:

$$dP = \frac{d^3 r_0 \; dE_0}{V} \cdot \frac{d\Omega_0}{4\pi} \cdot e^{-\mu_0 \ell_1} \cdot n_e^{eff} \frac{d\sigma_0^c}{d\Omega_1} d\Omega_1 d\ell_1 \cdot e^{-\mu_1(\ell_1' + \ell_2)} \cdot \left(dP^c + dP^e + dP^g\right) \cdot \Theta_V \tag{1}$$

where $d\Omega_i = d\varphi_i d\theta_i \sin\theta_i$ stands for the ith solid angle as defined in the ith reference system. For convenience the ith reference system is defined with its center at r_i and its z-axis aligned along $\vec{r}_i - \vec{r}_{i-1}$. The linear attenuation coefficient for photons of energy E_i inside the detection planes is denoted as μ_i. We will also use the linear attenuation coefficients associated to the different interactions, eg. μ_i^e for the case of photo-electric effect, indicating in this case the interaction in the superscript. The distance travelled by the photon inside the plane p is denoted as ℓ_p and the total distance travelled by a photon of energy E_k inside any plane will be denoted as λ_k. Thus, $\lambda_0 = \ell_1$, $\lambda_1 = \ell_1' + \ell_2$ and so on. The n_e^{eff} stands for the effective number density of electrons for the material of the detector planes ($LaBr_3$ in our case). The $d\sigma_i^c/d\Omega_j$ stands for the usual Klein–Nishina formula with the subscript indicating the energy of the photon, E_i. Finally, Θ_V is equal to 1 if $\vec{r}_0$ and E_0 are inside V and 0 otherwise. After these definitions, each term in equation (1) can be easily understood. The first term is the probability that the emission takes place inside the elementary volume $d^3 r_0 dE_0$ within V. The second term stands for the probability of emission of the photon from $\vec{r}_0$ with angles θ_0 and φ_0. The third term stands for the probability of the photon to penetrate ℓ_1 in the first plane. The fourth term stands for the probability of a Compton scattering in ℓ_1 with final emission angles θ_1 and φ_1. The fifth term stands for the probability of escaping the first plane and penetrating ℓ_2 in the second plane. The next terms stand for the differential probability of the photon to undergo in ℓ_2 a Compton, photo-electric or pair-production interaction. The last term stands for the fact that we only consider emissions from inside V and it will be useful as a book-keeping artifact for integration limits (see equation (9)). Specifically, for the Compton and photo-electric interactions:

$$dP^c = n_e^{eff} \frac{d\sigma_1^c}{d\Omega_2} d\Omega_2 d\ell_2 \cdot e^{-\mu_2 \ell_2'}, \qquad dP^e = \mu_1^e d\ell_2, \tag{2}$$

where in the first case we have included the probability of escape of the scattered photon, since the model considers only events with one photon interaction in each detector plane. Similarly, for the pair-production the escape probability of the two annihilation photons must also be considered. In this case we use the expression

$$dP^g = \mu_1^g d\ell_2 \frac{d\Omega_\gamma}{4\pi} e^{-\mu_e \ell}, \tag{3}$$

where Ω_γ stands for the angles of the direction that contains the two annihilation photons and ℓ is the total length traversed in the second plane by them. As a first approximation, these photons are taken as collinear, with energy $E_e = m_e c^2 = 511$ keV, and being created at the point of creation of the positron.

Although the detection probability of an emitted photon, dP, is properly described by equation (1), for the numerical implementation of the image reconstruction algorithm, it is convenient to express dP as much as possible in terms of measured variables. As a first step in this direction, the variables Ω_i and $d\ell_i$ are defined in terms of the $\vec{r}_i$ variables: $d\Omega_i d\ell_{i+1} = d^3 r_{i+1} / |\vec{r}_{i+1} - \vec{r}_i|^2$

$$dP(\vec{r}_0\vec{r}_1\vec{r}_2\ldots|V) = \frac{d^3r_0dE_0}{V}\frac{d^3r_1}{4\pi|\vec{r}_1-\vec{r}_0|^2}\frac{d^3r_2}{|\vec{r}_2-\vec{r}_1|^2}e^{-\mu_0\lambda_0}n_e^{eff}\frac{d\sigma_0^c}{d\Omega_1}e^{-\mu_1\lambda_1}\cdot \cdot\left(n_e^{eff}\frac{d\sigma_1^c}{d\Omega_2}d\Omega_2e^{-\mu_2\lambda_2}+\mu_1^e+\mu_1^g\frac{d\Omega_\gamma}{4\pi}e^{-\mu_e\ell}\right)\Theta_V. \tag{4}$$

At this point, we take advantage of the fact that this expression is well-suited for computing the sensitivity probability, i.e. the probability that an emission in V is detected (in any form). Thus, integrating equation (4) over all the possible outcomes

$$S_V = \int_V\frac{d^3r_0dE_0}{4\pi V}\int_{P_1}d^3r_1\frac{e^{-\mu_0\lambda_0}}{|\vec{r}_1-\vec{r}_0|^2}\int_{P_2}d^3r_2\frac{e^{-\mu_1\lambda_1}}{|\vec{r}_2-\vec{r}_1|^2}n_e^{eff}\frac{d\sigma_0^c}{d\Omega_1}\cdot \cdot\left(\int_{\Omega_2}d\Omega_2n_e^{eff}\frac{d\sigma_1^c}{d\Omega_2}e^{-\mu_2\lambda_2}+\mu_1^e+\mu_1^g\int_{\Omega_\gamma}\frac{d\Omega_\gamma}{4\pi}e^{-\mu_e\ell}\right) \tag{5}$$

where the first integrals are extended to the volumes of the voxel, $V=\Delta x\Delta y\Delta z\Delta E_0$, and the detection planes, P_i. The second integrals represent the escaping probability of photons generated after the interaction in the second plane, and add up all the possible outgoing angles of the photon after the Compton scatter and the angle of the two annihilation photons. Equation (5) allows computing the sensitivity matrix without having to resort to the very expensive conventional method of computing and summing all the possible cones of response (see below). The last integration in equation (5) will be referred to as the *double escape probability*, $S(\vec{r}_2)$ in the following, and it represents the probability that the two photons escape after being created at $\vec{r}_2$ inside the second plane.

Another variable that can be expressed in terms of measured variables is the polar angle, θ_1. Since θ_1 equals the Compton scattering angle in the first plane, then $d^3r_0=d\varphi\ \sin\beta d\beta\ d\xi\xi^2$ can be expressed in terms of the energy measured in the first plane, $\tilde{E}_1$, by using Compton kinematics

$$\cos\beta = 1-\frac{m_ec^2\tilde{E}_1}{E_0(E_0-\tilde{E}_1)}. \tag{6}$$

Thus $\sin\beta\ d\beta = d\tilde{E}_1m_ec^2/(E_0-\tilde{E}_1)^2$, and similarly for the polar angle of the outgoing photon when there is a second Compton interaction, θ_2. Upon application of these changes of variables, and after integrating out those variables which are not measured, we obtain

$$\frac{dP_V}{d^3r_1d\tilde{E}_1d^3r_2d\tilde{E}_2} = \int\frac{dE_0}{4\pi V}\frac{e^{-\mu_1\lambda_1}}{|\vec{r}_2-\vec{r}_1|^2}\frac{m_ec^2}{(E_0-\tilde{E}_1)^2}n_e^{eff}\frac{d\sigma_0^c}{d\Omega_1}\ T^{ceg}\ C \tag{7}$$

where T^{ceg} encodes the kinematics of the second interaction

$$T^{ceg} = \frac{m_ec^2}{(E_0-\tilde{E}_1-\tilde{E}_2)^2}n_e^{eff}\frac{d\sigma_1^c}{d\Omega_2}\int d\varphi_2e^{-\mu_2\lambda_2}+\mu_1^e\delta(E_0-\tilde{E}_1-\tilde{E}_2) + \mu_1^gS(\vec{r}_2)\delta(E_0-\tilde{E}_1-\tilde{E}_2-2m_ec^2) \tag{8}$$

and acts as a weight for the geometrical terms encoded in

$$C(\vec{r}_1,\vec{r}_2,\tilde{E}_1,E_0) = \int_0^{2\pi}d\varphi\int_0^\infty d\xi\ e^{-\mu_0\lambda_0}\Theta_V = \sum_{n=1}^{N_r\to\infty}\frac{2\pi}{N_r}\Delta\xi^{(n)}e^{-\mu_0\ell_1^{(n)}}. \tag{9}$$

It represents the integration of the smooth-varying function $e^{-\mu_0\lambda_0}$ over a surface defined by the intersection of a cone and (the spatial extent of) voxel V. The cone surface corresponds to the usual cone surface of Compton-based systems: the cone axis is given by $\vec{r}_1-\vec{r}_2$ and the aperture angle β is obtained from E_0 and $\tilde{E}_1$ (equation (6)). We will refer to this surface as *Cone of Response*, CoR, associated to the measured event $\{\vec{r}_1,\tilde{E}_1,\vec{r}_2,\tilde{E}_2\}$. The integral can be obtained by discretizing the values of φ, ($d\varphi\approx\Delta\varphi=2\pi/N_r$). This amounts to decompose the conical surface in a high number of rays, N_r. The value can be found by summing all the individual contributions of each ray, where $\Delta\xi^{(n)}$ stands for the length of the nth ray contained in the voxel and $\ell_1^{(n)}$ stands for the length of the nth ray contained inside the first detection plane.

Clearly, equation (7) describes a system with perfect energy and intrinsic spatial resolution. To take into account the actual resolutions, the usual convolutions with the functions describing the resolution models must be applied.

Finally, equation (7) can be interpreted as the probability of an emission from voxel[1] V, around $\vec{r}_0$ and E_0, being detected by the telescope as an event given by $\{\vec{r}_1,\tilde{E}_1,\vec{r}_2,\tilde{E}_2\}$; therefore, equation (7) constitutes the sought mathematical expression for the SM elements of our system.

[1] Actually, V need not be voxel-shaped. It represents a general integration volume in the $(\vec{r}_0,E_0)$ space.

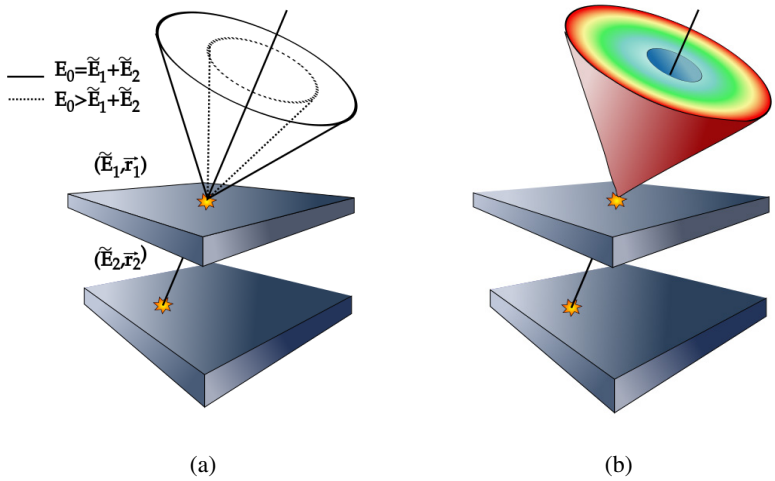

Figure 2. Diagram of the different CoRs that arise from one coincidence event. (a) Shows the decrease in the cone aperture angle as the initial energy increases. (b) Represents qualitatively the variation in the probability of different initial energies.

2.2. Implementation of the method

The main step in the image reconstruction process is the calculation of the SM. The SM rows are built for each measurement. For a measurement $\{\vec{r}_1, \tilde{E}_1, \vec{r}_2, \tilde{E}_2\}$, only the voxels with $E_0 \geqslant \tilde{E}_1 + \tilde{E}_2$ will be activated. For each of these energies, a different CoR is constructed, with an aperture angle given by equation (6). From that equation, for a fixed $\tilde{E}_1$, the Compton scattering angle decreases as the initial energy increases, and so the CoR with maximum aperture angle will be obtained for $E_0 = \tilde{E}_1 + \tilde{E}_2$, as illustrated in figure 2(a). Since the binning of the energy dimension in the field of view (FoV) is chosen with a fixed number of elements, only discrete values of E_0 are used, and the response function for every measurement is a set of CoRs with different aperture angles. Because the individual CoRs correspond to different E_0, they also have different probabilities T^{veg}, which are calculated as defined by equation (8). Figure 2(b) represents qualitatively the different relative probabilities assigned to different E_0 for an arbitrary event.

In our implementation of equation (8), the δ functions are replaced by $\delta(E_0 - \tilde{E}) = \Theta(\tilde{E}; E_0, E_0 + \Delta E_0)/\Delta E_0$, so that they are activated if the event energy $\tilde{E}$ falls within the voxel of energy E_0 and width ΔE_0. In the processing of individual events, the CoR associated to the photoelectric interaction is extracted assuming an incident energy of $\tilde{E}_1 + \tilde{E}_2$, and the corresponding voxels are filled. Equivalently, from the measured energies, the pair production CoR is obtained assuming an initial energy of $\tilde{E}_1 + \tilde{E}_2 + 2m_e c^2$. Lastly, all the possible CoRs related to a second Compton interaction are calculated, which correspond to initial energies in the range $[\tilde{E}_1 + \tilde{E}_2, E_{\max}]$, being $E_{\max}$ the maximum voxel energy considered in the FoV.

From equation (9), in order to assign the probabilities to the individual voxels in the FoV, the CoRs are modelled as a dense set of rays. The lengths of the rays traversing the voxels are calculated employing a conventional ray tracing technique (Siddon 1985). In the current implementation of the method, voxels not activated by any ray are not considered in the reconstruction process.

Regarding the sensitivity matrix, it is computed via Monte Carlo integration of equation (5). One beneficial feature of employing Monte Carlo integration is that it provides an estimation of the integral error, which decreases with the number of integration samples N as $1/\sqrt{N}$. The sensitivity matrix must be calculated specifically for the chosen FoV and geometrical configuration of the camera. In this work, the three contributions corresponding to each of the interactions in the second plane are computed separately. The final sensitivity is calculated as their sum and saved for future use in the image reconstruction process.

In our implementation, the double escape probability function $S(\vec{r}_2)$ is precomputed by dividing the detector volume into small elements and calculating the escape probability numerically through conventional Monte Carlo techniques. The values are stored in a look-up table and called during the computation of the system and sensitivity matrices.

For the numerical calculation of all the discussed probabilities, the values of μ for the detector material at the different energies are obtained from the National Institute of Standards and Technology (NIST) database (Berger *et al* 2010).

Finally, image reconstruction is performed with a List Mode Maximum Likelihood Expectation Maximization algorithm.

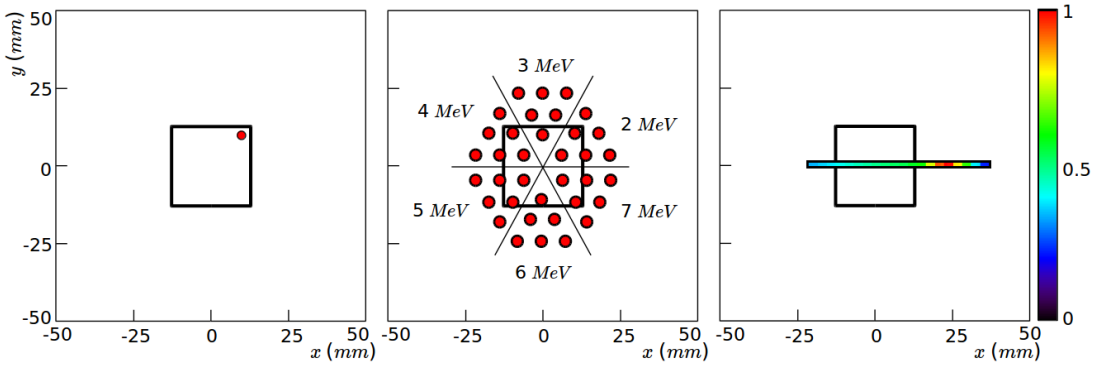

Figure 3. Diagram of the simulated sources. From left to right: point-like sources, discrete energy phantom and continuous energy phantom, where the different colours indicate the variation of activity. The black square indicates the detector footprint.

2.3. Image treatment

Since the implemented method yields four-dimensional images, the results must be integrated over some of the dimensions prior to its graphical representation. In this work, we will refer as x and y to the spatial dimensions parallel to the detector surface, and as z to its perpendicular direction. In many cases, if the distance between the source and the detector is known, the FoV may be considered with only one bin along the z dimension, being in fact an image with two spatial and one spectral dimension. This is a practicality that allows the employment of a reduced FoV in the reconstruction, thus decreasing the computational burden. As a first approximation, we follow this approach to test the imaging capacity of the algorithm. In order to recover the spatial distribution of the source, the energy domain must be integrated out; conversely, the reconstructed spectrum is obtained by integrating over the whole spatial domain, and mixed spatial-spectral representations result from integration over a single spatial dimension. The number of iterations in the reconstruction algorithm was optimized for each source distribution. The iterative process was stopped based on the visual appreciation of the images, after convergence was reached and before noise amplification. Unless otherwise specified, the images shown in this work correspond to iteration 20, which fulfilled the previous conditions. For a smoother visualization, all images presented in this work have been post-processed with a Gaussian filter with a sigma equal to one voxel length.

2.4. Sources employed for image reconstruction

2.4.1. Simulated data

The described implementation of the spectral reconstruction algorithm has been tested with different simulated sources. The simulated data have been obtained with GATE version 7.0 (Jan *et al* 2004), a Monte Carlo simulation toolkit based on Geant4 (Agostinelli *et al* 2003). Version 7.0 of GATE was employed in order to maintain consistency with the software employed in Muñoz *et al* (2018), although no significant changes are expected with more recent release versions. Several sources of increasing complexity have been simulated (see figure 3):

- *Point-like sources*. Six sources were simulated, all placed at the same position within the footprint of the detector surface, displaced 10 mm from its center in the x and y directions. Each of the sources emitted isotropically $4 \cdot 10^9$ monoenergetic photons in the range [2, 7] MeV, with a difference of 1 MeV between sources.
- *Discrete energy phantom*. This phantom consists of six regions of different energy emission, ranging from 2 to 7 MeV with a difference of 1 MeV between regions. The different regions are formed by six spherical sources with 2 mm radius, each emitting isotropically $4 \cdot 10^8$ photons. The separation between the centers of any neighbouring sources is 8 mm.
- *Continuous energy phantom*. This phantom emits in a continuous spectrum between 2 and 7 MeV, with a constant emission probability for the whole energy range. The spatial distribution of this phantom is inspired in the overall shape of the Bragg peak produced by a proton beam. All gammas are emitted following a thin linear path and the intensity increases until it reaches a peak, where it quickly drops. For this phantom, a total of $2 \cdot 10^{10}$ emitted photons were simulated.

The simulated Compton camera reproduces the experimental prototype. It consists of two identical planes of $LaBr_3$ with dimension $25.8 \times 25.8 \times 5\,mm^3$, as in the experimental prototype described in Barrio *et al* (2017). The distance between the centers of the planes is set to 50 mm and all the simulated sources are placed at a distance of 70 mm from the first plane. In all cases, the simulated data have been reconstructed in a 4D FoV of $101 \times 101 \times 1$ spatial voxels of $1\,mm^3$ and 99 spectral voxels, linearly distributed in the range [0.05, 9.95] MeV.

Once the simulated data are generated, an external sorter is applied in order to select the events in time coincidence that are used for image reconstruction. For the simulated tests carried out in this work, only the signal events have been considered, i.e. those produced by the combination of a Compton scatter in the first plane and a subsequent interaction in the second one by a single primary gamma. Reversed order events, produced by a Compton scatter in the second plane and a second interaction in the first one, have not been included in the reconstruction process. In all cases, the detector was simulated with perfect energy resolution. Given the output of the simulation produced by GATE, several approaches can be taken in the post-processing of the time coincidence events. On the one side, it provides access to all the physical interactions produced during the simulation, by both the primary gammas and the produced secondary particles. The information of an individual interaction is named *hit*, and it contains the precise, yet experimentally inaccessible, information of the generated data. On the other side, it also produces a collection of *singles* data, that congregate all the processes undergone by the primary and its secondary particles at one interaction point. From the singles list, the measurement information can be extracted as it would be measured experimentally, in which the total energy deposited by all particles constitutes the measured energy and the interaction position inside the crystal is given by a a weighted average over all energy depositions. However, in the two described data sets, it is also possible that the recoil electron produced in the Compton scattering escapes the detector material, taking part of the energy deposited by the initial gamma in the interaction. In Compton imaging, this energy loss causes a wrong assignment of the aperture angle at the considered E_0, thus leading to image artifacts. In order to avoid this effect, a third set of events, referred to as *ideal hits*, was extracted from the simulations. This last set of data takes the same interaction positions of the photons given by the hits, and forces the complete detection of the energy deposited in the first Compton interaction, so that all the energy transferred by the incident photon is preserved.

2.4.2. Experimental data

The algorithm has also been tested with experimental data. In the laboratory, data were measured with two gamma sources, ^{22}Na and ^{88}Y, with an activity of 847 and 506 kBq, respectively, placed on a plane parallel to the detector surface and separated a distance of 40 mm. Data were taken simultaneously with both sources, which combined provide the emission of four different gamma energies. The ^{22}Na spectrum has two emission peaks at 511 and 1275 keV, and ^{88}Y emits at the energies of 898 and 1836 keV. These data were produced in a previous experiment, whose results, evaluated with a non-spectral reconstruction algorithm, have been published in Muñoz *et al* (2017). In addition, an experimentally measured high energy source was also reconstructed. The employed data were taken at the HZDR Dresden, which provides a quasi-monoenergetic source of 4.44 MeV photons. The details of the experiment are published in Muñoz *et al* (2018b).

3. Results

3.1. Evaluation of the sensitivity model

The quality of the final reconstructed images depends on the sensitivity model. In this work, a sensitivity matrix specific for the employed FoV is computed before the image reconstruction process is initiated. The sensitivity images are obtained through numerical integration of equation (5), as described in section 2.2. Figure 4 shows the images calculated for the sensitivities to the different types of interactions (photoelectric, Compton or pair production) in the second plane. Since the employed FoV is four-dimensional, so is the sensitivity matrix. In figure 4, the resulting images are integrated to give two-dimensional images. In the top row images, the energy domain is integrated out, showing that the three contributions have similar spatial distributions. In the images in the bottom row, where the spectral dimension is preserved, it can be seen that the possible physical processes causing the detection in the second plane lead to very different distributions of probability. The integrated images of the final sensitivity matrix employed, given by the sum of the three contributions, are shown in figures 4(d) and (h).

In order to validate the physical model used in the numerical computation of the sensitivity matrix, the sensitivity at two spatial positions has been calculated through Monte Carlo simulations for the energy range [0.2, 7] MeV. For this validation, events with multiple interactions in a single plane or with reverse sequence have not been included, and only ideal signal events have been considered. Figure 5 shows that the values obtained from the simulations match the ones calculated with equation (5) for the three different contributions.

3.2. Reconstruction of simulated sources

3.2.1. Point-like sources

Images were reconstructed using the three data sets described in section 2.4.1. The number of coincidence events generated from the simulations for each source was 26 952, 21 194, 19 927, 15 928, 14 780 and 13 858, from lowest to highest energy. The reconstructed images of all sources with the three data sets are shown in figure 6(a). Figure 6(b) shows the spectra obtained after integration over the spatial domain of the reconstructed images.

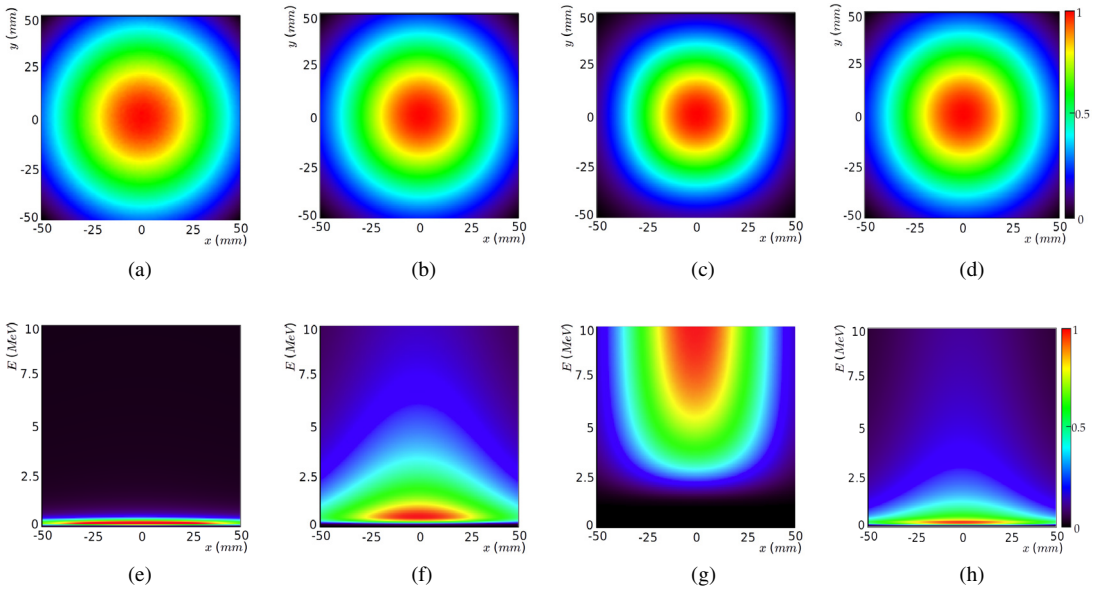

Figure 4. Figures in the top row show the sensitivities to the different interactions in the second plane, integrated over the spectral dimension: photoelectric (a), Compton (b), pair production (c) and total (d). Figures in the bottom row show the images integrated over the *y* axis: photoelectric (e), Compton (f), pair production (g) and total (h). The colour code in each image is normalized independently.

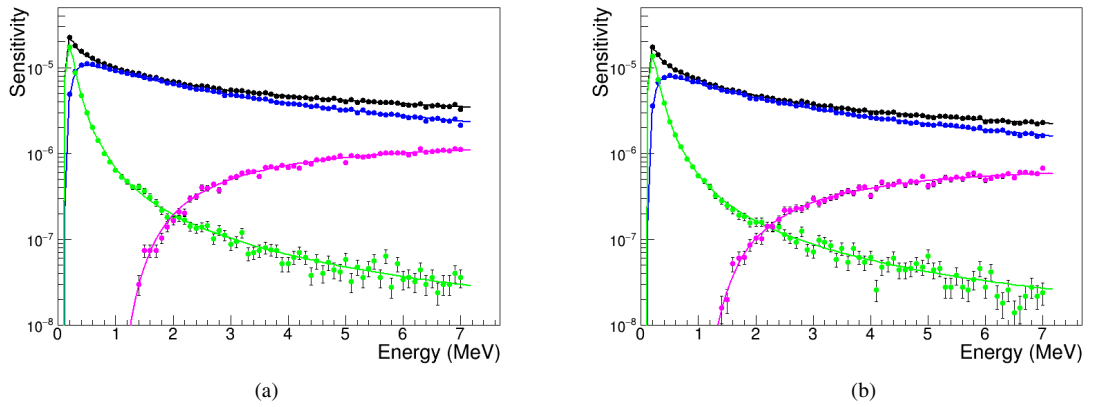

Figure 5. Sensitivity to the possible interactions of the photon in coincidence events over a range of energies for a source placed at $x = 0$ mm (a) and $x = 30$ mm (b). The points are obtained from simulated data and the continuous lines from the integration of equation (5). The different colours indicate the interaction experienced by the photon in the second plane: Compton scatter (blue), photoelectric absorption (green), pair production (pink) or any of the three (black).

In order to compare the distributions obtained from the different data sets, the intensity of each distribution is normalized to its own maximum. In the three cases, intensity maxima were recovered at the simulated energies. However, the plot shows that the values obtained for sources with higher energies are not correctly reconstructed for the singles data. An improvement is seen when the hits data are selected, and the reconstruction with the ideal hits set assigns the correct intensity to all the tested energies. Figure 6(c) shows the same results with the three described data sets, but, in this case, the intensities are not the result of the integration over the whole spatial domain; instead, they are calculated by summing the values of the voxels containing the sources and their immediate neighbours. The neighbours are defined as the voxels placed immediately next to the voxel with maximum value, in all spatial and spectral dimensions. This allows a better estimation of the intensity assigned around the exact source positions.

3.2.2. Discrete energy phantom

The phantom was reconstructed employing the three data sets from the simulation with 49 337 signal events. Several interesting aspects can be pointed out from the four dimensional reconstructed image. In the first place, the integration over the spectral domain yields a purely spatial image. The corresponding images are shown in figure 7(a), in which all the individual sources are identified. Here, the degradation of the spatial image at higher

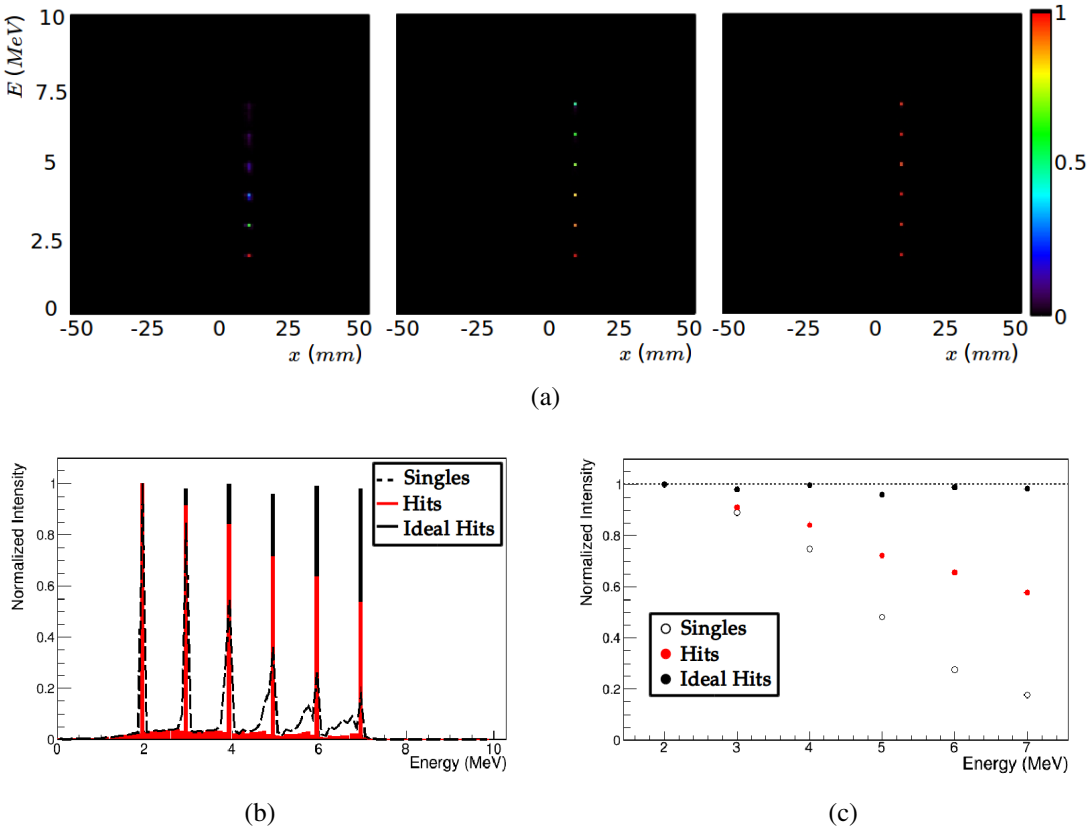

Figure 6. Reconstructed images obtained for the different sets of data from the simulations after integration over the *y* spatial direction (a). Spectra after integration over the spatial domain of the whole reconstructed images (b) and intensities of only the voxels containing the sources and their immediate neighbours (c).

energies can be observed, which is only correctly compensated with the ideal hits data set. In the second place, slices of specific energies can be extracted from the resulting image. In figure 7(b), slices for the minimum and maximum emitted energies are shown to illustrate how the different regions of emission are reconstructed at their corresponding energies. Finally, when the image is integrated over the spatial domain, a reconstruction spectrum is obtained (figure 7(c)), which contains a distinct peak of intensity at each of the different energies emitted by the phantom. Again, the degradation of the image at higher energies is evident in the spectra recovered for the singles and hits data sets. Looking at the ideal hits spectrum shown in figure 7(c), it can be noted that the intensity is still somewhat higher at the lower energies. This small difference arises because, for each of the source energies, a residual tail of intensity appears at energies below the true emission, caused by the events with partial energy deposition: since the algorithm needs to test all possible energies, some intensity is spread into the energies between the measured value and the true emission. Given that this spread extends towards lower energies, the cumulative value of the tails induced by all sources causes an increase in the lower energy intensities. Nevertheless, the difference between the 2 and 7 MeV peaks is below 10% of the maximum value, showing that the method can accurately reconstruct the ideal events. Another visible feature in the ideal hits spectrum is that the recovered peaks are wider than those shown in figure 6(b). This is due to the application of a Gaussian filter to the reconstructed image in this case. Since in our case we have 4D images, the filter is applied to both the spatial and the spectral components of the image.

3.2.3. *Continuous energy phantom*

Images of the phantom were reconstructed, for the three simulated data sets, with 70 631 signal events and 10 iterations. The corresponding images can be seen in figure 8. The spatial distribution of the emission is represented in figure 8(a), where the simulated intensity is compared to the reconstructed profiles in the *x* (left) and *y* (center) dimensions. Regarding the spectral results, the spectra recovered with the different data sets and the simulated emission are plotted in figure 8(a)(right). The two-dimensional reconstructed spatial images are also shown in figure 8(b). The continuous energy range of emission can also be appreciated in figure 8(c), in which mixed spatial-spectral images obtained after the integration of only one spatial dimension are represented. From these representations, it can be seen that the reconstructed activity is distributed in the emitted spectral range, although the assigned intensity is very degraded for high energies with the singles and hits data sets. The results are clearly improved when ideal hits are employed, achieving a distribution similar to the simulated spectrum.

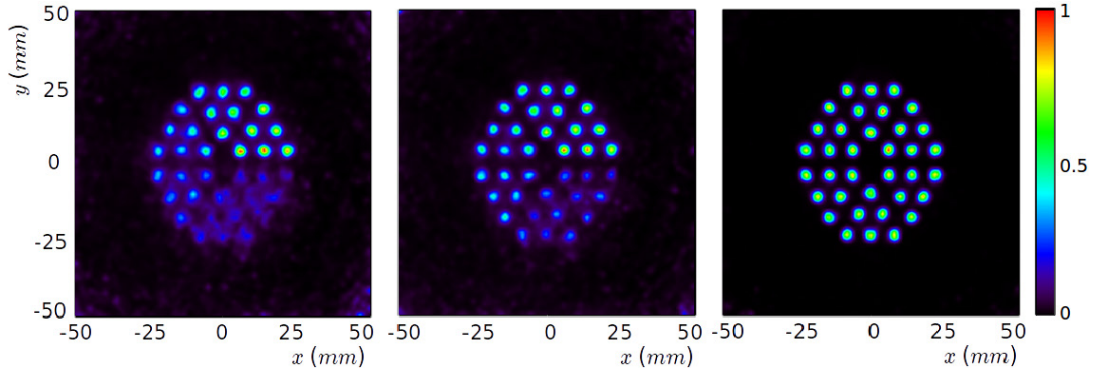

(a)

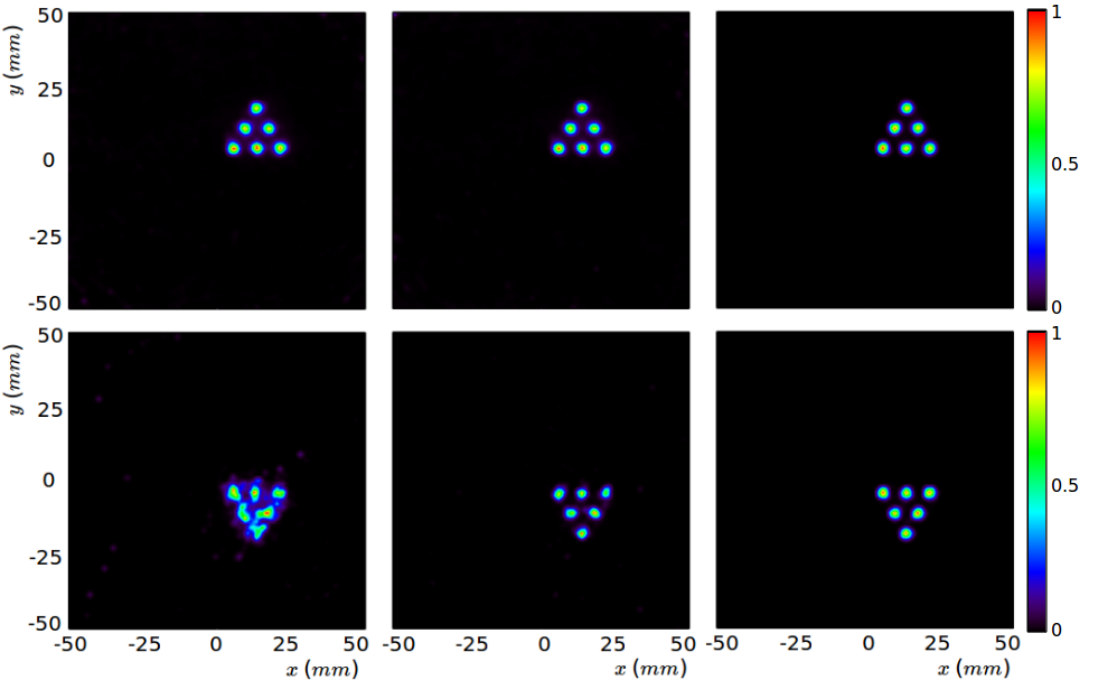

(b)

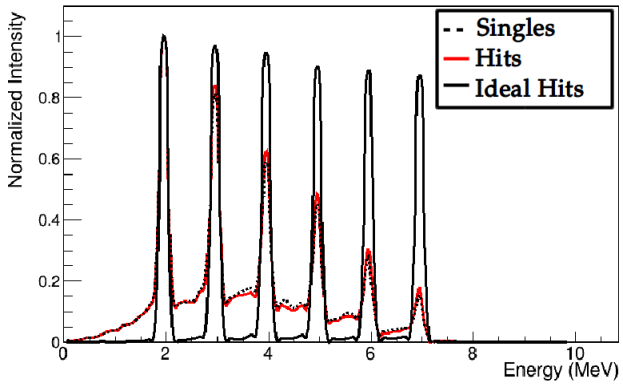

(c)

Figure 7. Images reconstructed for the discrete energy phantom with the different data sets. (a) Spatial images after integration over the energy domain. From left to right: singles, hits and ideal hits. (b) Slices selected for the regions of 2 (top row) and 7 MeV (bottom row). From left to right: singles, hits and ideal hits. (c) Reconstructed spectra after integration over the spatial domain.

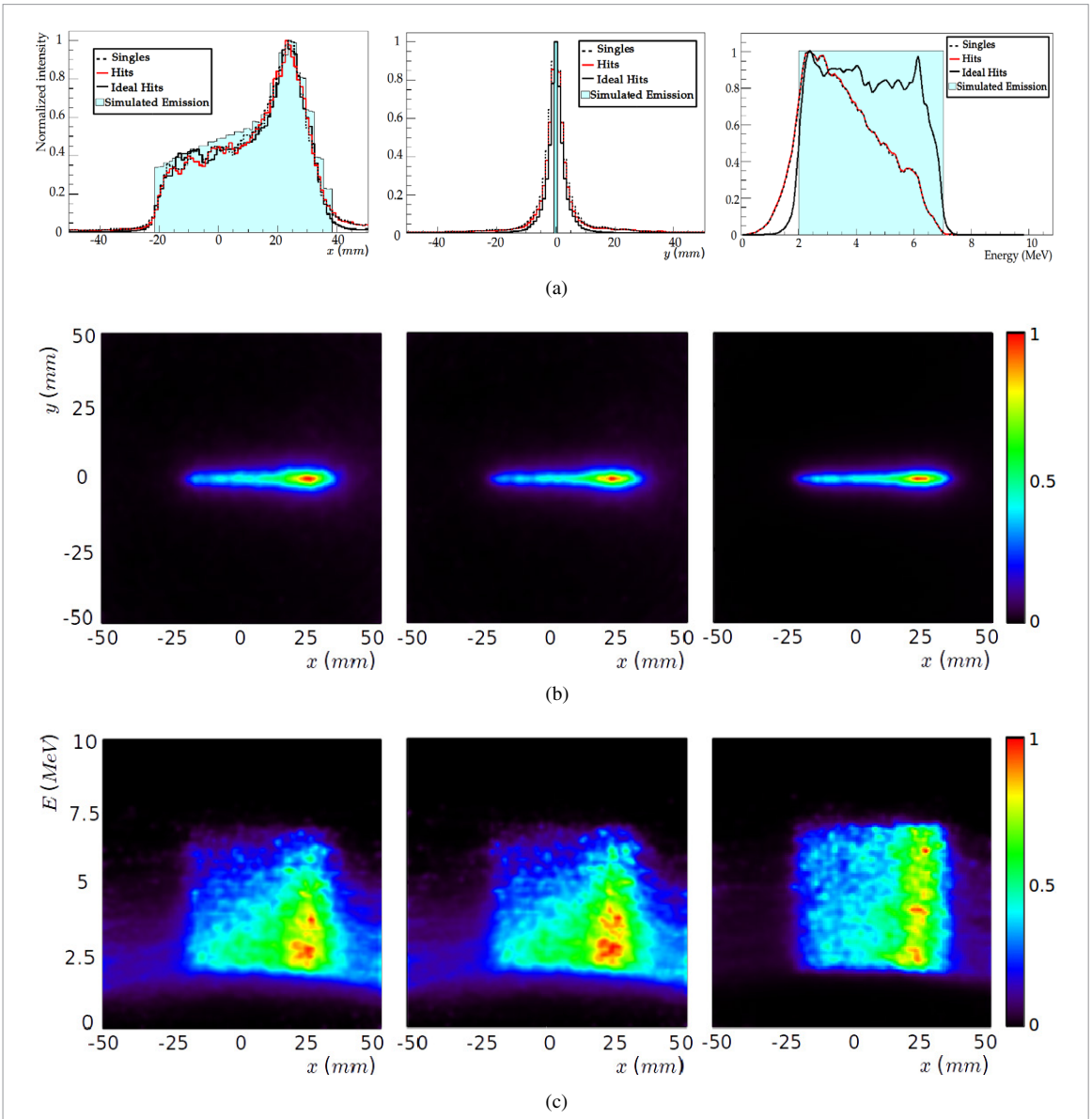

Figure 8. Results obtained for the homogeneous energy phantom with the three data sets. (a) Profiles of the emitted and reconstructed distribution of activity in the x (left) and y (center) spatial directions, and reconstructed spectra after integration over the spatial domain (right). (b) Spatial images after integration over the energy domain. From left to right: singles, hits and ideal hits. (c) Spatial-spectral images after integration over the y spatial dimension. From left to right: singles, hits and ideal hits.

The results obtained with this phantom show that the spatial distribution is accurately reconstructed in the three cases. However, the spectral information is degraded for the singles and hits data, in which the intensity at high energies is underestimated, and the simulated emission can only be recovered from the ideal hits data.

3.3. Reconstruction of experimental sources

During the measurement with the ^{22}Na and ^{88}Y sources, 63 101 events were detected in time coincidence. These data were reconstructed employing a FoV of 101 × 101 × 1 spatial voxels of 1 mm^3 and 100 spectral voxels, linearly distributed in the range [0.05, 2.55] MeV. The results obtained from the reconstructed four-dimensional image can be seen in figure 9. Figures 9(a) and (b) show, respectively, the spectral-integrated image and the slices extracted at the four different energy peaks. In them, the two different radioactive sources can be identified, and it can be appreciated that, as expected, the two energies emitted by each source yield an image that peaks at the same position. Figure 9(c) shows a comparison between the measured summed energy spectrum, obtained by summing the energy deposited in both planes for every coincidence event, and the recovered spectrum given by the spatial integration of the reconstructed image. The peaks corresponding to the emitted energies are more prominent in the recovered spectra, due to the events with only partial deposition in the summed energy spectrum that are reconstructed with the appropriate initial energy. The third plot in figure 9(c) shows the spectra recovered when the integration of the image is performed only over the spatial voxels containing the position of each of the sources, where their respective emitted energies are clearly identified. In the reconstructed spectra,

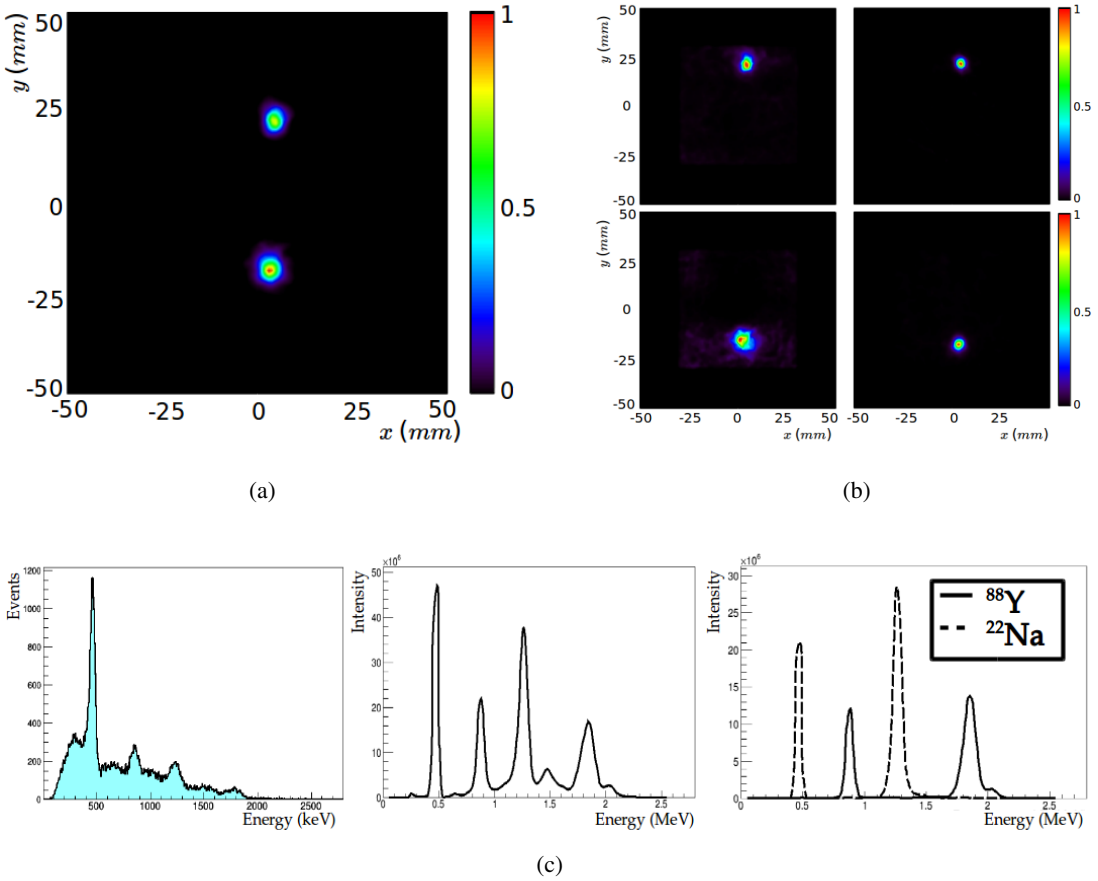

Figure 9. Reconstructed image of the ^{22}Na and a ^{88}Y sources together. (a) Spatial image, integrated over the spectral domain. (b) Spatial slices at the peak energies of the two sources. Top: ^{88}Y source, summed between 875–925 keV (left) and 1800–1850 keV (right). Bottom: ^{22}Na source, summed between 475–525 keV (left) and 1250–1300 keV (right). (c) Comparison of the spectra. Left: measured spectra obtained by summing the energy depositions of the coincidence events in both planes. Center: reconstructed spectra after integration over the whole spatial domain of the reconstructed image. Right: reconstructed spectra after integration over the spatial domain only for the voxels located at the positions of the sources.

the intensity of the different peaks is related to the emission activity of the corresponding energies, although they cannot be directly compared. According to the decay scheme of ^{22}Na, the number of emitted 511 keV photons should be roughly twice the number of 1275 keV photons, while the ^{88}Y source emits roughly the same number of 898 keV and 1836 keV photons. Given the activity of the measured sources, the number of detected 898 keV and 1836 keV photons should be approximately 60% of that from 1275 keV photons. Looking at the peak heights corresponding to each energy in the reconstructed spectrum, it can be seen that in the experimental results, in contrast to the simulations, the intensity is somewhat underestimated for the lower energies. This is due mainly to two experimental limitations that are not considered by the method. The first of them is the detector energy resolution, which leads to a bigger uncertainty in the calculated Compton scattering angle of lower energy photons, causing their activity to be reconstructed with a wider spread across voxels. The second one is the experimental low energy threshold, which was about 70 keV for each detector plane. This energy threshold determines the smallest scattering angle that can be detected, which is larger for lower energy photons. Given the limited detector surface, smaller scattering angles are more likely to impinge on the second plane, an effect that favours the detection of higher energy photons and limits significantly the number of detected events from lower energies. In addition, since in this case the tested energies are much lower than in simulations, the effect of escaping recoil electrons is not significant.

Finally, figure 10 shows the combined spatial-spectral view of the reconstructed image after integration over the spatial x dimension, where the four peaks are visible in the spatial and spectral domains simultaneously.

In order to test the algorithm with experimental data measured at high energies, we employed a set of data measured from a monoenergetic source of 4.44 MeV. A four dimensional image was reconstructed employing 7543 coincidence events in a FoV of $101 \times 101 \times 1$ spatial voxels of 1 mm^3 and 100 spectral voxels, linearly distributed between 0.05 and 9.95 MeV. The resulting image, integrated over the spectral domain, is shown in figure 11(a). Figure 11(b) represents the comparison between the measured summed energy spectrum and the spectrum recovered from the reconstructed image. It is worth noting that the initial gamma energy, 4.44 MeV, has a low probability of being completely absorbed in the detector, and thus the measured spectrum does not show a

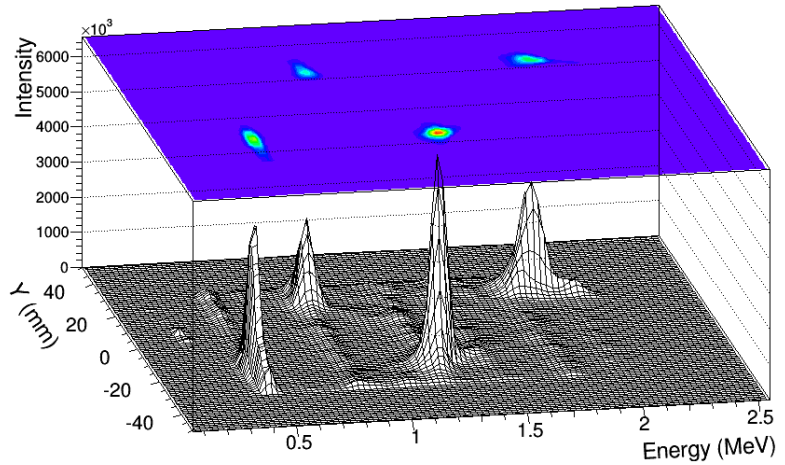

Figure 10. Reconstructed image of the ^{22}Na and a ^{88}Y sources together after integration over the x spatial dimension.

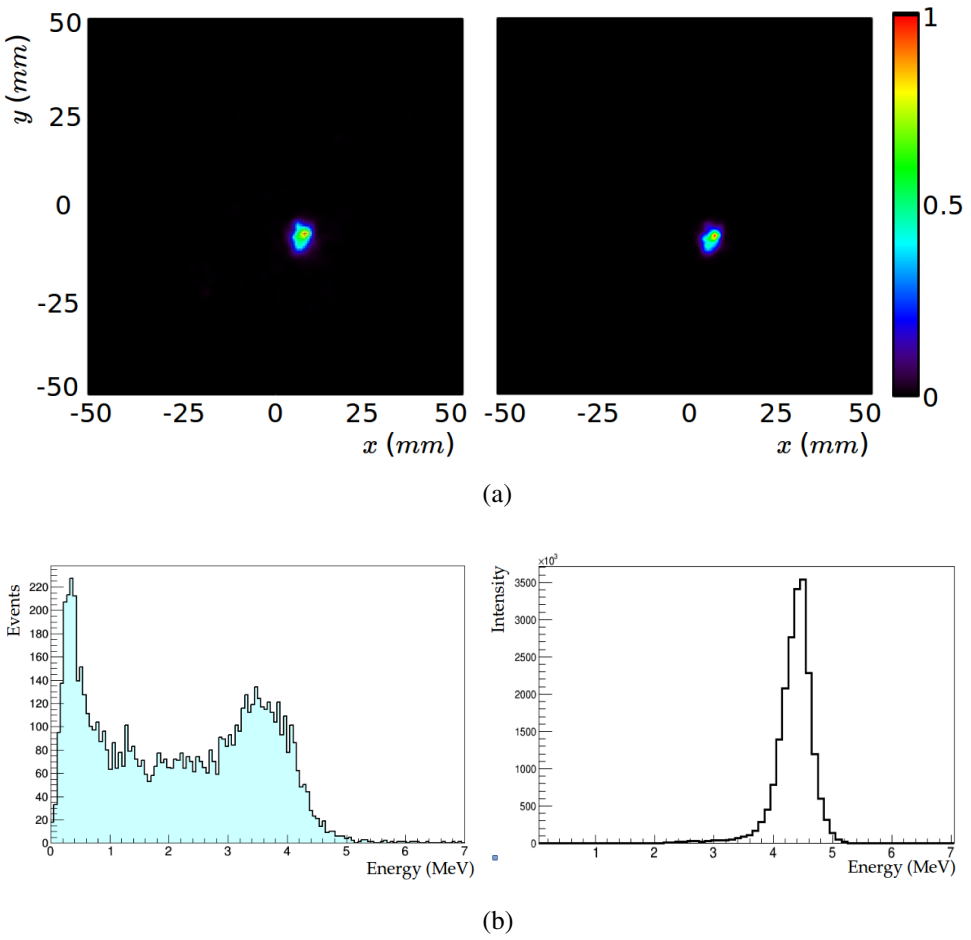

Figure 11. Results obtained with experimental data measured from a 4.439 MeV gamma source. (a) Reconstructed image after integration over the spectral domain (left) and spatial slice at 4.4 MeV (right). (b) Measured summed energy spectrum (left) and reconstructed spectrum recovered after integration over the spatial domain (right), where a peak is clearly visible at 4.4 MeV.

clear peak at that position. Nevertheless, in the spectrum obtained from the reconstructed image, a peak is recovered precisely at the energy emitted by the source.

Images have been obtained from experimental data measured with photons of five different energies. Although a complete resolution study (Gong *et al* 2016) is out of the scope of this paper, the width of the reconstructed images in the spatial and spectral domains can be quantified in order to compare the performance of the method in the tested energy range. Table 1 shows the full width at half-maximum of the reconstructed images. The spatial values are obtained from a Gaussian fit to the x and y profiles through the image maxima, and the spectral values from Gaussian fits to the peaks in the reconstructed spectra.

Table 1. Spatial and spectral FWHM of the reconstructed experimental sources.

Energy (MeV)	$FWHM_{x,y}$ (mm)	$FWHM_E$ (MeV)	$FWHM_E$ / E (%)
0.511	6.5, 5.6	0.05	9.8
0.898	5.1, 5.5	0.07	7.8
1.275	4.3, 4.8	0.09	7.1
1.836	3.8, 4.0	0.13	7.1
4.439	4.1, 4.4	0.52	11.7

4. Discussion

A spectral reconstruction algorithm for two-plane Compton cameras is proposed and tested in this work. The main concept behind its development is the possibility to associate partial depositions of energy in the second interaction with a probability for a range of plausible incident gamma energies, which in turn yield a set of CoRs with their corresponding aperture angles. In order to do so, the SM is divided into the three possible interactions that can produce a detection in the second detector plane: photoelectric absorption, a second Compton scattering or an $e^- e^+$ pair production. Since the reconstruction is performed on a four dimensional FoV, during the iterative algorithm those voxels that contain both the spatial position and the spectral emission of the source are obtained.

Given the strong dependence of the detection probability on the energy and the position of the emission point of the photons, the employment of an accurate sensitivity matrix becomes necessary for the algorithm to be able to correctly position the source, in both the spatial and the spectral domains. Here the physical model is also used to derive an expression for a four dimensional sensitivity matrix, which is calculated via Monte Carlo integration. The accuracy of the proposed sensitivity matrix has been verified through a comparison with the sensitivity values obtained from simulations with GATE with good agreement. The use of an accurate sensitivity matrix allows image reconstruction in the FoV beyond the footprint of the detector.

The performance of the proposed algorithm has been evaluated through image reconstruction of data from a variety of simulated sources. Images were first reconstructed using the singles list, which are ideal events that can be regarded as a good approximation of the best possible accessible events measured by a detector with perfect energy and intrinsic spatial resolution. Even at the singles level, the quality of the reconstructed images is lower than expected. In order to investigate where the information is lost, more ideal data sets have been employed. Images were reconstructed from the hits data set, in which the spatial coordinates are the exact interaction positions and with the energy measured by the detector. Although this set improves the singles results, the recovered images are not fully compensated. For that reason we consider the ideal hits, employing also the exact energy lost by the gamma. In this ideal case, both the spectral and the spatial information are successfully recovered. Therefore, the algorithm performs correctly under the assumption of ideal measurements, but when singles or hits are used the reconstructed images are degraded.

From the study with point-like sources, two important factors have been found to degrade the reconstruction process at high energies with the singles and hits data sets. The first of them is the displacement of the electron dispersed in the Compton scatter from the interaction position. This displacement grows larger for higher incident energies, and it can cause an error in the position of the apex and a misalignment in the axis of the CoRs. The second and most important factor, closely related to the first one, is the missing energy carried away by escaping electrons. As the incident energy increases, so does the probability that the dispersed electron escapes the detector, taking part of the energy lost by the primary gamma. This fact can produce various effects: if an electron escapes the first detector plane, the measured energy $\tilde{E_1}$ will be smaller than that transferred in the Compton scatter, and thus the aperture angles of the CoRs will be larger than they should; if an electron escapes the second detector plane, the CoR constructed for the actual emitted energy will still reach the source position, but its probability will be wrongly assigned. Furthermore, if an electron escapes one of the planes and reaches the other, it could trigger a false coincidence event that would add noise to the reconstructed image. Only when ideal hits from the simulations were selected, these effects were avoided and the reconstruction code was able to reconstruct all the sources and fully correct their intensities; when more realistic events are used, the obtained spectra tend to underestimate the intensity at high energies, although the spatial information is still successfully recovered.

In order to test the performance of the algorithm in a more demanding scenario, two more complex phantoms have been defined. In the discrete energy phantom, the obtained images show that the algorithm is able to reconstruct simultaneously different individual sources at their position and energy of emission when ideal data are employed. For more realistic data, although the intensity is not correctly compensated in all the energy range, in the spatial image all the sources at the different energy regions are identified. In all cases, the recovered spectra obtained from the integration of the images over the spectral domain show one peak at each of the emitted energies.

The results obtained with the continuous energy phantom show the method performance with a source distributed continuously in both spatial and spectral domains. Regarding the spectral information, the reconstructed activity is distributed in the emission energy range; however, the intensity is again underestimated at high energies, especially when singles and hits data are employed. Nevertheless, in the spatial domain, the algorithm was able to find in all cases the start and end points of emission in a line-distributed source, as well as the position of the peak of activity, all of them important features in prospective reconstruction of the prompt gamma creation maps during irradiation. This can be seen in the reconstructed line profiles, which in the three cases are very similar to the simulated distribution.

Finally, the reconstruction algorithm was also used with experimental data from different incident gamma energies. The tests with the two ^{22}Na and ^{88}Y sources together demonstrate the applicability of the proposed method for spectral identification of radioactive sources. By selecting the spatial slices at each of the four gamma energies emitted, the position of the sources is determined. As expected, at the two energies corresponding to one of the sources the locations of the voxels with highest probability coincide. Another visible feature is that the lower emitted energies yield noisier images, which can be attributed to their higher probability of producing a backscatter coincidence event with wrong ordering (events that are backscattered in the second plane and subsequently detected in the first one). Comparing the measured summed energy spectrum to the one recovered from the reconstructed image, it can be seen that the algorithm is able to find the incident energy of those events with partial energy depositions. This behaviour is even more noticeable in the case of a 4.4 MeV gamma source. At this energy, the probability of total energy deposition is reduced, and the measured summed energy spectrum offers little information about the incident energy of the measured photons. When the spectral reconstruction code is used, only those CoRs generated with the actual emitted energy produce a coherent image and the spectral information of the source can be recovered. From the resolution results listed in table 1, the performance of the method at different energies can be analyzed. In the four low energies measured in the laboratory, a trend towards better spatial resolution at higher energies can be identified. Regarding the spectral performance, although the total width of the peak increases for higher energies, the value of the energy resolution function ($\Delta E/E$) improves for higher energies in this range. Finally, a worse spectral resolution was obtained with 4.4 MeV gammas. This could be due to the effect of escaping recoil electrons, as seen from the simulated studies. The probability of escaping electrons was negligible at the low energies measured in the laboratory, but they could be responsible for the widening of the recovered peak at this high energy.

From the study with all simulated sources, we have shown that the algorithm can work successfully, but its performance with the singles data is limited. The missing energy carried away by electrons escaping the detector has been identified as an important source of image degradation, which causes the reconstructed intensities to be more underestimated for higher energy sources. This effect is present at the gamma energies involved in hadron therapy, and should therefore be addressed in order to achieve a spectral reconstruction. A possible experimental approach would be the use of a tracking system for the recoil electron. A recoil electron tracking system is used in other prototypes of Compton cameras employing gas chambers (Kabuki *et al* 2010, Mizumoto *et al* 2015) or stacks of silicon detectors (Bhattacharya *et al* 2004, Andritschke *et al* 2005, Frandes *et al* 2010, Thirolf *et al* 2016) as scatterers. In those cases, the electron track is essentially used to obtain the electron recoil angle, which can be used to constrain the photon scattering angle to a fraction of the cone surface. Applied to our case, a tracking system would allow identifying events with escaping electrons and taking them into account. If this effect could be modelled, its inclusion in the calculation of the system matrix would correct the weight assigned to the different elements, and thus the reconstructed intensities. In that sense, a more complete study to model the recoil electron escaping probability is also foreseen. Other aspects not yet considered in the current implementation of the method are the detector spatial and energy resolutions. One way to account for the detector resolutions is to extend each CoR according to the uncertainties in the measurement, as described in Gillam *et al* (2012) and Muñoz *et al* (2018). However, in approaches based on ray tracing techniques, these models require in general more sampling rays, thus increasing the computational burden and reconstruction time. Indeed, computation time is a crucial factor in online monitoring methods, and the current implementation must still be optimized. Lastly, the method has yet to be evaluated with data measured from particle beams at clinical conditions.

5. Conclusions

The proposed method can be employed for image reconstruction of data measured by a two-plane Compton camera, irrespective of the prior information about the energy of the detected gammas. The algorithm has been shown to successfully reconstruct the different source distributions tested in this work, obtained both from simulations and experimental measurements, which is a promising step towards the use of this device in hadron therapy treatment monitoring. However, we have seen that the method can only reconstruct completely the spectral and spatial distributions under the assumption of ideal measurements, and image degradation appears when simulated singles or hits are employed. The missing energy carried away by electrons escaping the detector

has been identified as the major source of image degradation, which needs to be specifically addressed either in the experimental design or in the system matrix. Despite its current limitations, the spatial distributions of complex phantoms has been recovered in all cases. Finally, the method is able to accurately reconstruct point-like experimental sources, recovering simultaneously both their emission spectrum and spatial location.

Acknowledgments

This work was supported in part by the European Commission's 7th Framework Programme through the ENVISION project (G A num 241851), by the Spanish Ministerio de Ciencia, Innovación y Universidades (FPA2017-85611-R and IFIC's Center of Excellence Severo Ochoa SEV-2014-0398) and by H2020 ENSAR2-MediNet (project number 654002). Group members are supported by Ramón y Cajal, Severo Ochoa Excelellence postdoctoral contract, UVEG Atracció de Talent and Generalitat Valenciana contracts.

References

Agostinelli S *et al* 2003 Geant4—a simulation toolkit *Nucl. Instrum. Methods Phys. Res.* A **506** 250–303

Andritschke R, Zoglauer A, Kanbach G, Bloser P F and Schopper F 2005 The Compton and pair creation telescope MEGA *Exp. Astron.* **20** 395–403

Barrio J, Etxebeste A, Granado L, Muñoz E, Oliver J, Ros A, Roser J, Solaz C and Llosá G 2017 Performance improvement tests of MACACO: a Compton telescope based on continuous crystals and SiPMs *Nucl. Instrum. Methods Phys. Res.* A **912** 48–52

Berger M, Hubbell J, Seltzer S, Chang J, Coursey J, Sukumar R, Zucker D and Olsen K 2010 *Xcom: Photon Cross Section Database (Version 1.5)* (Gaithersburg, MD: National Institute of Standards and Technology)

Bhattacharya D, ONeill T, Akyüz A, Samimi J and Zych A 2004 Prototype TIGRE Compton γ-ray balloon-borne telescope *New Astron. Rev.* **48** 287–92

Dogan N and Wehe D 1994 Optimization and angular resolution calculations for a multiple Compton scatter camera pp 269–73

Draeger E, Mackin D, Peterson S, Chen H, Avery S, Beddar S and Polf J 2018 3D prompt gamma imaging for proton beam range verification *Phys. Med. Biol.* **63** 035019

Frandes M, Zoglauer A, Maxim V and Prost R 2010 A tracking Compton-scattering imaging system for hadron therapy monitoring *IEEE Trans. Nucl. Sci.* **57** 144–50

Gillam J, Lacasta C, Torres-Espallardo I, Juan C C, Llosá G, Solevi P, Barrio J and Rafecas M 2011 A Compton imaging algorithm for on-line monitoring in hadron therapy *Medical Imaging 2011: Physics of Medical Imaging* vol 7961 (International Society for Optics and Photonics) (https://doi.org/10.1117/12.877678)

Gillam J *et al* 2012 Simulated one pass listmode for fully 3D image reconstruction of Compton camera data *Nuclear Science Symp. and Medical Imaging Conf.* (IEEE) (https://doi.org/10.1109/NSSMIC.2012.6551752)

Golnik C *et al* 2016 Tests of a Compton imaging prototype in a monoenergetic 4.44 MeV photon field—a benchmark setup for prompt gamma-ray imaging devices *J. Instrum.* **11** P06009

Gong K, Cherry S R and Qi J 2016 On the assessment of spatial resolution of PET systems with iterative image reconstruction *Phys. Med. Biol.* **61** N193

Jan S *et al* 2004 GATE: a simulation toolkit for PET and SPECT *Phys. Med. Biol.* **49** 4543

Kabuki S *et al* 2010 Electron-tracking Compton gamma-ray camera for small animal and phantom imaging *Nucl. Instrum. Methods Phys. Res.* A **623** 606–7

Kormoll T, Fiedler F, Schöne S, Wüstemann J, Zuber K and Enghardt W 2011 A Compton imager for *in vivo* dosimetry of proton beams—a design study *Nucl. Instrum. Methods Phys. Res.* A **626, 627** 114–9

Krimmer J, Dauvergne D, Létang J and Testa É 2018 Prompt-gamma monitoring in hadrontherapy: a review *Nucl. Instrum. Methods Phys. Res.* A **878** 58–73

Kroeger R A, Johnson W N, Kurfess J D, Phlips B F and Wulf E A 2002 Three-Compton telescope: theory, simulantions, and performance *IEEE Trans. Nucl. Sci.* **49** 1887–92

Kurosawa S *et al* 2012 Prompt gamma detection for range verification in proton therapy *Curr. Appl. Phys.* **12** 364–8

Llosá G, Barrio J, Cabello J, Crespo A, Lacasta C, Rafecas M, Callier S, de La Taille C and Raux L 2012 Detector characterization and first coincidence tests of a Compton telescope based on $LaBr_3$ crystals and SiPMs *Nucl. Instrum. Methods Phys. Res.* A **695** 105–8 (New Developments in Photodetection NDIP11)

Maxim V, Lojacono X, Hilaire E, Krimmer J, Testa E, Dauvergne D, Magnin I and Prost R 2016 Probabilistic models and numerical calculation of system matrix and sensitivity in list-mode MLEM 3D reconstruction of Compton camera images *Phys. Med. Biol.* **61** 243

Min C H, Kim C H, Youn M Y and Kim J W 2006 Prompt gamma measurements for locating the dose falloff region in the proton therapy *Appl. Phys. Lett.* **89** 183517

Mizumoto T *et al* 2015 New readout and data-acquisition system in an electron-tracking Compton camera for MeV gamma-ray astronomy (smile-ii) *Nucl. Instrum. Methods Phys. Res.* A **800** 40–50

Muñoz E *et al* 2018b Tests of MACACO Compton telescope with 4.44 MeV gamma rays *J. Instrum.* **13** P05007

Muñoz E, Barrio J, Bernabéu J, Etxebeste A, Lacasta C, Llosa G, Ros A, Roser J and Oliver J F 2018 Study and comparison of different sensitivity models for a two-plane Compton camera *Phys. Med. Biol.* **63** 135004

Muñoz E, Barrio J, Etxebeste A, García-Ortega P, Lacasta C, Oliver J, Solaz C and Llosá G 2017 Performance evaluation of MACACO: a multilayer Compton camera *Phys. Med. Biol.* **62** 7321

Parajuli R K, Sakai M, Kada W, Torikai K, Kikuchi M, Arakawa K, Torikoshi M and Nakano T 2019 Annihilation gamma imaging for carbon ion beam range monitoring using Si/CdTe Compton camera *Phys. Med. Biol.* **64** 055003

Peterson S W, Robertson D and Polf J 2010 Optimizing a three-stage Compton camera for measuring prompt gamma rays emitted during proton radiotherapy *Phys. Med. Biol.* **55** 6841–56

PTCOG 2019 Patient statistics and facilities under operation. particle therapy co-operative group (www.ptcog.ch)

Roellinghoff F *et al* 2011 Design of a Compton camera for 3D prompt-γ imaging during ion beam therapy *Nucl. Instrum. Methods Phys. Res.* A **648** S20–3 (*NIMA 4th Int. Conf. on Imaging techniques in Subatomic Physics, Astrophysics, Medicine, Biology and Industry*)

Rohling H, Priegnitz M, Schoene S, Schumann A, Enghardt W, Hueso-González F, Pausch G and Fiedler F 2017 Requirements for a Compton camera for *in vivo* range verification of proton therapy *Phys. Med. Biol.* **62** 2795
Schumann A, Petzoldt J, Dendooven P, Enghardt W, Golnik C, Hueso-González F, Kormoll T, Pausch G, Roemer K and Fiedler F 2015 Simulation and experimental verification of prompt gamma-ray emissions during proton irradiation *Phys. Med. Biol.* **60** 4197
Siddon R L 1985 Fast calculation of the exact radiological path for a three-dimensional ct array *Med. Phys.* **12** 252–5
Solevi P *et al* 2016 Performance of MACACO Compton telescope for ion-beam therapy monitoring: first test with proton beams *Phys. Med. Biol.* **61** 5149
Thirolf P *et al* 2016 A Compton camera prototype for prompt gamma medical imaging *EPJ Web of Conf.* **117** (Nuclear Structure)
Verburg J M, Riley K, Bortfeld T and Seco J 2013 Energy- and time-resolved detection of prompt gamma-rays for proton range verification *Phys. Med. Biol.* **58** L37–49
Wilderman S J, Fessler J A, Clinthorne N H, LeBlanc J and Rogers W L 2001 Improved modeling of system response in list mode EM reconstruction of Compton scatter camera images *IEEE Trans. Nucl. Sci.* **48** 111–6
Xu D and He Z 2007 Gamma-ray energy-imaging integrated spectral deconvolution *Nucl. Instrum. Methods Phys. Res.* A **574** 98–109